




Photoionization microscopy in the time domain: Classical atomic chronoscopyP. Kalaitzis,¹ S. Danakas ¹, K. Ferentinou,¹ S. Cohen ¹ and C. Bordas ^{2,*}¹*Atomic and Molecular Physics Laboratory, Physics Department, University of Ioannina, 45110 Ioannina, Greece*²*Université de Lyon, Université Claude Bernard Lyon 1, CNRS, Institut Lumière Matière, F-69622 Villeurbanne, France*

(Received 19 April 2024; accepted 26 June 2024; published 15 July 2024)

The glory effect is one of the characteristic manifestations of the divergence of the classical scattering cross section, which occurs whenever the deflection function goes through zero for a nonzero impact parameter. This effect, companion of the more frequently discussed rainbow effect, occurs in particular in atomic photoionization in the presence of an external electric field, where it manifests itself by the appearance of an intense peak at the center of the photoelectron momentum distribution transversely to the field. Above the field-free ionization threshold where solely continuum Stark states exist (while quasibound ones are absent), the intensity of the glory signal, extracted from high-resolution momentum distribution images, oscillates as a function of energy. These oscillations exhibit a spectral frequency that increases with increasing energy, and Fourier analysis allows the extraction of time-dependent information from them. In this work we present a detailed analytical study of the dynamical aspects of classical electron trajectories in atomic Rydberg states in the presence of an external electric field. We demonstrate the strong connection between those classical properties and the spectral signatures of the glory signal. This close link provides a brilliant illustration of the correspondence principle in a complex situation where the quantum system is in the continuum and exhibits characteristic frequencies that vary with the excitation energy.

DOI: [10.1103/PhysRevA.110.013112](https://doi.org/10.1103/PhysRevA.110.013112)**I. INTRODUCTION**

The electron motion in bound atomic Rydberg states constitutes an internal clock of arbitrarily adjustable frequency. Owing precisely to its bound nature, however, it is not directly accessible other than via a destructive procedure, typically following a pump-probe ionization scheme. By contrast, the electron motion, and particularly its time properties, may be, at least in principle, directly measured when continuum atomic states are involved. In the case of a free atom, without any external influence, the intrinsic properties of the electron clock are in general lost and no time information may be extracted, apart from the trivial time of flight of the free electron upon photoionization. On the contrary, nontrivial time information can be obtained when an external static (dc) electric field is applied, giving rise, under certain circumstances, to Stark resonances in the continuum. This leads to a situation where one has, at the same time, a free electron that can be detected, and a complex and tunable time dependence arising from the peculiar properties of the motion in the combined Coulomb and external dc fields. Therefore, Stark states in the continuum just above threshold offer a measurable electron clock, with an intrinsic degree of control, the electronic energy E , and an additional external degree of control, the static electric field strength. Though potentially accessible, limitations in time responses of detectors imply that the direct measurement of time properties of the electronic motion is hardly achievable. However, characteristics

directly linked to this internal clock are more easily accessible in the spectral domain, where short time corresponds to wide spectral spacing. This is a rather general feature of atomic or molecular spectra: energy spacings are inversely proportional to the classical frequencies of the internal atomic or nuclear motion. In the present case, however, we are not dealing with a fixed frequency (e.g., molecular rotation or vibration) but rather with sliding frequencies, changing with the degree of excitation.

The peculiarity of our approach is that instead of recording a simple Stark spectrum in the continuum, we record complete 2D maps of the electron momentum. These maps display the measured electron signal as a function of both the energy E and the electron momentum transversely to the dc field (see for example Ref. [1]). They provide complex 2D information exhibiting composite spectral structures from which time information may be recovered. The global treatment of these maps is beyond the scope of the present work and will be the subject of future efforts. In the present paper we focus exclusively on one of the most characteristic features of these data, namely the glory oscillation. The glory signal corresponds to electrons with null transverse momentum and manifests itself as an intense peak at the center of the photoelectron momentum distribution images. The glory effect is a common feature of atomic scattering. Similarly to the rainbow effect, it is the signature of the divergence of the classical scattering cross section. Whereas the rainbow results from an extremum in the deflection function, the glory effect appears when the deflection function cancels out while the impact parameter is nonzero [2]. More precisely, in the present case, the glory signal occurs when the transverse electron momentum is zero

*Contact author: christian.bordas@univ-lyon1.fr

for a nonzero (or non- π) value of the electron ejection angle β with respect to the external electric field. Classical and semiclassical glory scattering has been described in some detail [3] in the case of photoionization microscopy (PM) [4]. In addition, a recent PM experiment employing two-photon ionization of ground-state Mg atoms [5] showed that the glory signal exhibits strong oscillations and beating effects over an appreciable energy range below, as well as above, the static-field-free ionization limit. In fact, a comparison with a two-photon ionization hydrogenic model revealed that many features of the process are essentially atom independent. Complex time information was extracted from the glory spectrum and compared to the numerically computed time dependence of classical electron trajectories. In particular, it was shown that the experimental glory spectrum carries a signature of the classical time-of-flight differences among the several trajectories associated with the glory effect, which can be extracted by Fourier analysis of the glory spectrum.

The main purpose of the present work is to provide a comprehensive analysis of the dynamical aspects of classical electron motion in the combination of a Coulomb and a static electric field \mathbf{F} . We provide all the details on the analytical calculation of classical time delays that were not previously available in the literature. Through these results and hydrogenic quantum calculations it is subsequently demonstrated quantitatively that glory oscillations in the ionization continuum of an atom in the presence of \mathbf{F} indeed exhibit striking signatures of the electron motion clock.

The paper is organized as follows. In Sec. II we describe the experimental framework in which our subsequently developed calculations are embedded, introducing both the experimental principles and the definitions of the parameters and variables that will be used in the following. In Sec. III, we summarize the properties of classical trajectories and explicitly develop analytical expressions for classical times of flight in the context of photoionization. In Sec. IV, the quantitative calculation of the glory angles (launch angles corresponding to electron trajectories contributing to the glory signal) and of the corresponding times of flight are presented. The latter are also discussed in connection with the simple case of photodetachment. These results are subsequently compared in Sec. V, with an exact calculation performed in the framework of nonrelativistic quantum theory following an approach similar to the one used in Ref. [5], namely by comparing calculated classical time delays with the Fourier analysis of the calculated quantum glory spectrum. Finally, we conclude by giving some hints on possible continuations of this work.

II. PRINCIPLE AND BASIC DEFINITIONS

Although primarily theoretical, this paper is also deeply connected with laboratory experiments. Therefore, it is crucial to introduce the experimental principle underlying the present discussion and the definitions of basic quantities used in the following. It should be stressed that the reasoning developed in this work only arises in situations where we are able to spatially resolve the electron current resulting from photoionization of a simple atomic system in the presence of a static electric field, or more precisely, to accurately map the electron momentum perpendicular to the applied field.

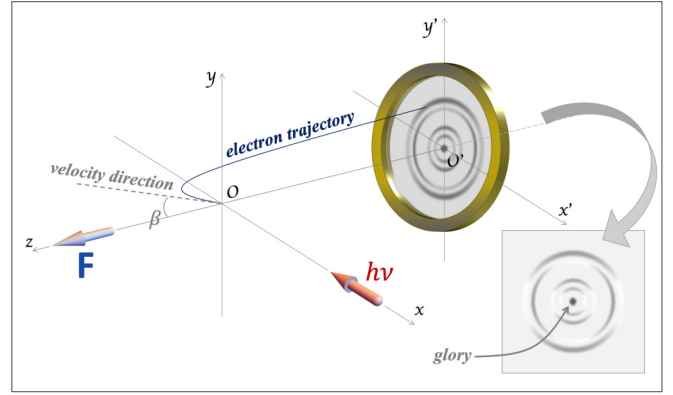


FIG. 1. Schematic principle of the experiment. The atom interacts with photons of energy $h\nu$ at the center O of a velocity map imaging spectrometer (VMIS). Electrons are ejected at a launch angle β with respect to the electric field \mathbf{F} and are further detected on a position-sensitive detector (PSD). The PSD is made of a tandem microchannel plate (MCP) detector followed by a phosphor screen perpendicular to the electric field. Electron impacts are captured by a CCD camera and accumulated over several thousand laser shots in order to build the image. See text for details.

By spatial resolution we mean that not only the classical envelope of the photoelectron current is measured, but also its intimate structure arising from quantum interferences. These conditions correspond strictly to what is defined as photoionization microscopy, an experimental method introduced first as a thought experiment by Russian physicists in the early 80s [6] that one of us has contributed to develop as an actual experimental method in the early 2000s [4].

A schematic view of the experiment is given in Fig. 1. Atoms are excited by a number of photons of energy $h\nu$ at the center O of a velocity-map imaging spectrometer (VMIS) [7] equipped with a magnifying lens [8]. The latter is not drawn in Fig. 1, but it represents a necessary addition for resolving the spatial modulation of the slow (0–100-meV) photoelectron current due to quantum interferences. The excitation laser beam is oriented along the O_x axis and perpendicular to the electric field \mathbf{F} of strength F present in the VMI and oriented along the O_z axis. This field is inhomogeneous by design. It may, however, be approximated by a homogeneous one over the very limited size of the interaction region. Upon absorption of N photons (most frequently one or two), according to the chosen excitation scheme, atoms are excited at energy E with respect to the ionization limit in the absence of the field (i.e., the zero-field ionization limit). In practice, E is chosen to lie just above the field-induced ionization threshold and, therefore, the electron is excited in the ionization continuum. Electrons are ejected at a launch angle β with respect to \mathbf{F} . The electrons are detected by a position-sensitive detector (PSD) made of tandem microchannel plates (MCPs) followed by a phosphor screen whose surface is perpendicular to the electric field. A charge-coupled device (CCD) camera records the 2D distribution of light spots on the screen. Recorded images are transferred to a PC, where they are accumulated over several thousand laser shots resulting in images of the photoelectron momentum distribution transversely to the electric field. The MCP detector is located at a distance $|z_{\text{det}}|$ from the excitation

point. The glory signal corresponds to the electron signal at the center O' of the image. Details about the actual implementation of this experimental principle were previously given in Refs. [1,9], as well as in Ref. [5] for the specific glory study, and, with the exception of the information that is absolutely relevant to the present study, we will not describe it any further.

III. PROPERTIES OF THE CLASSICAL MOTION

A. The classical Coulomb-Stark problem

Exact expressions for the classical electron trajectories under the combined action of an attractive nucleus (Coulomb field) and a homogeneous static electric field $\mathbf{F} = F\mathbf{z}$ have been amply detailed in earlier works. This classical problem is fully integrable, and the nature of the planar motion solutions was extensively studied by Beletsky [10] in the context of celestial mechanics. Demkov *et al.* adapted these solutions for situations related to atomic physics [6,11]. The peculiarities of the classical planar trajectories were subsequently analyzed in the context of slow photoelectron imaging [12,13] and photoionization microscopy [4,14,15]. However, in all of these previous photoionization-oriented works, attention was given only to the geometric properties of the trajectories, while explicit expressions for the electron time of flight were not provided. More recently, Lantoine *et al.* [16] studied the most general case of motion in the context of celestial mechanics, and introduced general analytical formulas for expressing satellite times of flight. Their results can be used in the context of atomic physics at the cost of several technical manipulations. This is exactly the central point of the present section, with particular attention on the analysis of the glory signal and the corresponding time delays.

To this end, let us briefly recall that for the Coulomb-Stark potential [6,11] given below (in atomic units, $\hbar = e = m_e = 1$),

$$V_{\text{CS}}(\mathbf{r}) = -Z/r + Fz, \quad (1)$$

with $r = [x^2 + y^2 + z^2]^{1/2}$, and Z the atomic charge of the ion core (hereafter set equal to $Z = 1$), the classical equations of electron motion are separable in parabolic coordinates [17,18]:

$$\xi = r + z \geq 0; \quad \eta = r - z \geq 0; \quad \phi = \tan^{-1}(y/x). \quad (2)$$

This separation requires the introduction of the reduced-time variable τ , related to the physical time variable t via the definition [11]

$$d\tau = dt/r. \quad (3)$$

The corresponding equations of motion and parametric expressions of ξ , η , and ϕ as a function of τ are given in the Appendix. In the following, we restrict the discussion to those trajectories where the electron is ejected and escapes from the Coulomb center towards the PSD, whose plane is perpendicular to the z axis and located at $z = z_{\text{det}} = -\eta_{\text{det}}/2 < 0$.

Note that $V_{\text{CS}}(\mathbf{r})$ exhibits a local maximum along the z axis [19]. This so-called saddle-point energy E_{sp} defines the boundary between the bound ($E < E_{\text{sp}}$) and the free ($E \geq E_{\text{sp}}$)

motion. It writes in atomic units as

$$E_{\text{sp}} = -2F^{1/2}. \quad (4)$$

The energy range $E \geq E_{\text{sp}}$ where ionization is classically allowed includes the zero-field ionization limit at $E = 0$. In addition, we define a dimensionless variable that will be used throughout the paper, namely the reduced energy ϵ :

$$\epsilon = \frac{E}{|E_{\text{sp}}|}. \quad (5)$$

Furthermore, it should be emphasized that the momentum p_ϕ along coordinate ϕ , that is, the projection of the orbital angular momentum on the dc-field axis, is a constant of motion. The quantum counterpart of p_ϕ is the magnetic quantum number m , as referenced with respect to the dc-field axis, which is a good quantum number of the quantum Stark problem. For $p_\phi \neq 0$ the glory effect cannot occur because nonzero centrifugal terms emerge in the equations governing $\xi(\tau)$ and $\eta(\tau)$ and prevent the presence of the electron on the z axis, just as they prevent the electron from being arbitrarily close to the core ($r = 0$). Hence, the glory effect appears only for $p_\phi = 0$ [3], this value corresponding to the planar electron motion and to a time-independent coordinate $\phi = \phi_0 = \text{constant}$. The discussion that follows is restricted to the $p_\phi = m = 0$ case, and the trajectory of an electron under the influence of $V_{\text{CS}}(\mathbf{r})$ is entirely determined by its initial position (ξ_0, η_0, ϕ_0) , its total energy E , and the angle β between its initial velocity and the field z axis. The initial position is assumed to be the origin $(\xi_0 = 0, \eta_0 = 0)$, i.e., at the center O of the Coulomb force at $r = 0$. The potential energy diverges at this point; however, this divergence does not imply any singularity in the electron motion in this specific case. Note that the launch angle is restricted to the interval $0 \leq \beta \leq \pi$, and from Fig. 1 we see that $\beta = 0$ denotes ejection along the field direction ($+z$) and $\beta = \pi$ ejection opposite to the field ($-z$) and towards the PSD plane.

B. Trajectories, reduced arrival times, and coordinates of impact on the detection plane

The analytical expressions $\xi(\tau)$ and $\eta(\tau)$ can be conveniently written solely in terms of the aforementioned angle β , the reduced energy ϵ as defined in Eq. (5) above, and the external electric field strength F . The complete expressions of $\xi(\tau)$ and $\eta(\tau)$ in the case of open motion (ionization) are given in the Appendix, Eqs. (A3)–(A11).

For $\phi = \phi_0 = \text{constant}$ the trajectory is confined to a plane inclined by ϕ_0 with respect to the $x - z$ plane. By further fixing the values of $Z = 1$, F , and ϵ , the trajectory towards the detector can be traced parametrically in τ and for any given angle β , in either parabolic $[\xi(\tau), \eta(\tau), \phi_0]$ or Cartesian coordinates:

$$\begin{aligned} x(\tau) &= [\xi(\tau) \eta(\tau)]^{1/2} \cos \phi_0 \\ y(\tau) &= [\xi(\tau) \eta(\tau)]^{1/2} \sin \phi_0 \\ z(\tau) &= [\xi(\tau) - \eta(\tau)]/2. \end{aligned} \quad (6)$$

It turns out that the motion of the electron along parabolic coordinate ξ is bound at any energy and periodic in τ , with period T_ξ whose expression is given explicitly in Eq. (A7).

In other words, the parabolic coordinate ξ is zero whenever $\tau = \tau_k = (k + 1)T_\xi$, with $k = 0, 1, 2, \dots$ a positive or zero integer. Furthermore, by making use of T_ξ , the trajectories may be conveniently parametrized by means of the dimensionless scaled reduced-time variable τ_d defined as the ratio

$$\tau_d \equiv \tau/T_\xi. \quad (7)$$

Along the η coordinate and for $-1 \leq \epsilon < 0$ the electron escapes and reaches the PSD only for the angles $\beta \geq \beta_c \equiv 2 \arcsin |\epsilon|$. For $\beta < \beta_c$ the electron does not escape from the attractive center, while for positive energies ($\epsilon \geq 0$) there are no such restrictions and $\beta_c = 0$. For the trajectories leading to ionization the reduced time required for the electron to reach the detector, i.e., the reduced arrival time, is denoted as $\tau = T_\eta$. Accordingly, the coordinates of electron impact on the detector plane located at a position $z_{\text{det}} < 0$ from the source are denoted as $\xi_{\text{det}} = \xi(T_\eta)$ and $\eta_{\text{det}} = \eta(T_\eta)$. Then, it holds that

$$\xi_{\text{det}} - \eta_{\text{det}} = -2|z_{\text{det}}|, \quad (8)$$

while the radius of impact on the detector is given by

$$\rho(F, |z_{\text{det}}|, \epsilon, \beta) = \sqrt{\xi_{\text{det}} \eta_{\text{det}}}. \quad (9)$$

$$T_\eta = \begin{cases} \frac{1}{F^{1/4}} \frac{1}{[2 \sin(\beta/2)]^{1/2}} \operatorname{arccn}\left(\frac{1-\Lambda}{1+\Lambda} |m_\eta\right) & \text{for } |\epsilon| \leq \sin(\beta/2) \\ \frac{1}{F^{1/4}} \frac{2^{1/2}}{[\epsilon + [\epsilon^2 - \sin^2(\beta/2)]^{1/2}]^{1/2}} \operatorname{arcsn}\left(\sqrt{\frac{\Lambda}{1+\Lambda}} |m_\eta\right) & \text{for } \epsilon \geq \sin(\beta/2) \end{cases} \quad (12a)$$

where arccn and arcsn denote inverse Jacobi elliptic functions [20], and m_η is given in Eq. (A11).

In the asymptotic approximation $|z_{\text{det}}| \rightarrow \infty$, the expressions of Eqs. (12a) and 12(b) merge with Eq. (A12) and become

$$T_\eta = T_\eta^\infty = \frac{2^{1/2}}{F^{1/4}} \frac{K(m_\eta)}{[\sin(\beta/2)]^{1/2}}, \quad (13)$$

where m_η is given by Eq. (A11a) and $K(m)$ is the complete elliptic integral of the first kind [20]. Equation (13) holds for $\epsilon \geq -1$.

By means of any of the above equations (12a), 12(b), or (13), and using expressions given in the Appendix, both parabolic ($\xi_{\text{det}}, \eta_{\text{det}}, \phi_0$) and Cartesian ($x_{\text{det}}, y_{\text{det}}, z_{\text{det}}$) coordinates of the electron impact point on the detector may be calculated.

C. Glory effect and glory angles

The distribution of photoelectron impacts on the PSD can be computed via ξ_{det} and η_{det} (and ϕ_0). For an isotropic electron source [12] and for the planar motion discussed here, it suffices to calculate the classical differential ionization cross section R as a function of the impact radius $\rho(F, |z_{\text{det}}|, \epsilon, \beta)$ on the detector. This is defined as [5]

$$R(\rho) \equiv \frac{d\sigma}{dA}(\rho) = \frac{\sigma_0}{4\pi} \sum_j \frac{\sin \beta_j}{\rho} \left| \frac{d\rho}{d\beta_j} \right|^{-1}, \quad (14)$$

where $dA = 2\pi \rho d\rho$ is the elementary detector surface and σ_0 is the total ionization cross section. The summation in Eq. (14)

In the general case of finite $|z_{\text{det}}|$, and given the complexity of the expressions for both coordinates [Eqs. (A3) and (A8)], the exact T_η value must necessarily be determined by numerical inversion. For most practical situations, however, the distance $|z_{\text{det}}|$ is many orders of magnitude larger than the typical atomic dimensions. When this holds one can apply the asymptotic approximation, $|z_{\text{det}}| \rightarrow \infty$. In practice it suffices for $|z_{\text{det}}|$ to be finite but large with respect to the absolute value of the location $z_{\text{sp}} = -F^{-1/2}$ of the saddle point at energy E_{sp} . Then, satisfactory analytical expressions for T_η may be found under the quite realistic $|z_{\text{sp}}| \ll |z_{\text{det}}|$ condition that remains valid even for small field strengths F , where $|z_{\text{sp}}|$ may become macroscopic. In turn, this finite- $|z_{\text{det}}|$ approximation implies also that $\eta_{\text{det}} \gg \xi_{\text{det}}$ and $\eta_{\text{det}} \gg \eta_+$, where η_+ [given in Eq. (A9)] denotes the ‘‘amplitude’’ of $\eta(\tau)$. Under this approximation Eq. (8) simplifies to

$$\eta_{\text{det}} \approx 2|z_{\text{det}}| \gg \eta_+; \text{ for } |z_{\text{sp}}| \ll |z_{\text{det}}|, \quad (10)$$

and by defining the ratio

$$\Lambda \equiv \frac{\eta_{\text{det}}}{\eta_+} \approx \frac{2|z_{\text{det}}|}{\eta_+} \gg 1, \quad (11)$$

we find that

$$\text{for } |\epsilon| \leq \sin(\beta/2) \quad (12a)$$

$$\text{for } \epsilon \geq \sin(\beta/2) \quad (12b)$$

runs over all ejection angles β_j leading to the same radius ρ . Glory scattering, resulting in a high-intensity central peak in the photoelectron images, occurs whenever $\rho(F, |z_{\text{det}}|, \epsilon, \beta)$ goes through zero while $\sin \beta \neq 0$ and Eq. (14) exhibits a singularity. Evidently, the angles $\beta = 0$ and $\beta = \pi$ cannot contribute to the effect, since then the conditions $\sin \beta = 0$ and $\rho \rightarrow 0$ are simultaneously fulfilled. For a given reduced energy ϵ , the contributions to the glory signal stem from the trajectories corresponding to launch angles leading to $\xi_{\text{det}} = 0$ (and $\rho = 0$), that is, to those trajectories whose source-to-detector reduced times-of-flight are an integer number of periods T_ξ [Eq. (A7)] along ξ . For the computation of these glory angles, it is convenient to use the number Q of ξ oscillations performed until the electron reaches the detector,

$$Q \equiv \frac{T_\eta}{T_\xi}. \quad (15)$$

The integer part of Q is the number of zeros of the function $\xi(\tau)$ along the electron trajectory, or in other words the number of crossings between the electron trajectory and the dc-field axis. Furthermore, the quantity Q also represents the maximum value of the aforementioned dimensionless scaled reduced-time variable τ_d defined in Eq. (7), i.e., $0 \leq \tau_d \leq Q$. If the source-to-detector distance $|z_{\text{det}}|$ is finite, Q may depend on it, as well as on the field strength F , and needs to be computed numerically. On the contrary, in the asymptotic limit of a detector at infinity ($\eta_{\text{det}} \rightarrow \infty$, $|z_{\text{det}}| \rightarrow \infty$) this quantity, labeled as Q^∞ , can be expressed analytically [see Eq. (A13)]. In either case, the glory angles

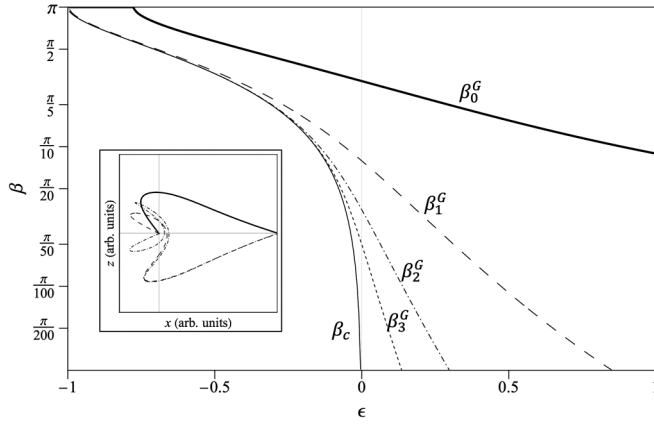


FIG. 2. Evolution of the glory angles $\beta_k^G(\epsilon)$ for $k=0-3$ and of the critical angle β_c as a function of the reduced energy ϵ . The trivial value $\beta = \pi$ is not plotted. The angle $\beta_0^G(\epsilon)$ is defined for $\epsilon \geq \epsilon_{0,\text{thr}} \approx -0.775$, while for $k \geq 1$ angles $\beta_k^G(\epsilon)$ are defined practically for all energies $\epsilon > -1$ [see Eq. (18)]. The logarithmic vertical scale is chosen in order to emphasize the large magnitude difference between the angles $\beta_k^G(\epsilon)$ as k increases. Inset: glory trajectories at $\epsilon = 0$ for glory orders $k = 0, 1$, and 2 .

$\beta_k^G(\epsilon)$ are given by the roots of the equations:

$$Q(F, |z_{\text{det}}|, \epsilon, \beta_k^G(\epsilon)) = k + 1, \quad k = 0, 1, 2, \dots \quad (16)$$

Note that since Q^∞ depends solely on ϵ and β , in the asymptotic limit the angles $\beta_k^G(\epsilon)$ depend on the field only implicitly through ϵ . Consequently $\beta_k^G(\epsilon)$ remains unchanged for any field value [in contrast to $\beta_k^G(E)$]. On the other hand, to the best of our knowledge, there are no analytical solutions of Eq. (16) and the solutions β_k^G need to be found in a purely numerical way. Nevertheless, it is easy to show that there is an energy threshold $\epsilon_{k,\text{thr}}$ for each glory-angle order, below which this angle cannot be defined. This threshold actually corresponds to the limit $\beta_k^G(\epsilon_{k,\text{thr}}) = \pi$, and for $|z_{\text{det}}| \rightarrow \infty$ one finds

$$K\left(\frac{1}{2} - \frac{\epsilon_{k,\text{thr}}}{2}\right) = \frac{2k}{\pi} \sqrt{\frac{2}{\epsilon_{k,\text{thr}}}}. \quad (17)$$

Numerical resolution of the above equation for the lowest orders gives

$$\begin{aligned} \epsilon_{0,\text{thr}} &\approx -0.775\,156 \\ \epsilon_{1,\text{thr}} &\approx -0.995\,642 \\ \epsilon_{2,\text{thr}} &\approx -0.999\,948 \dots \end{aligned} \quad (18)$$

Note that in earlier works [12,15], the threshold $\epsilon_{0,\text{thr}}$ was introduced as the onset of the so-called “direct” trajectories (defined as electron trajectories never crossing the z axis) and denoted as ϵ_{dir} . Also note that as soon as $k \geq 1$, angles $\beta_k^G(\epsilon)$ are defined for practically all energies $\epsilon \geq -1$. Figure 2 illustrates the general evolution of the various glory angles in the asymptotic limit as a function of the reduced energy in the range $[-1,1]$, together with the critical angle β_c defined above.

Typical (finite) glory trajectories are displayed in the inset to clarify the discussion. In practice, for calculations performed with a finite source-to-detector distance, glory angles are numerically calculated explicitly as a function of $|z_{\text{det}}|$, ϵ and F without any approximation.

Once the glory angles are known, one may obtain the corresponding reduced times-of-flight by introducing them into Eqs. (12a) and (12b), or (13). It is finally remarkable that when dealing with glory trajectories arriving at point O' , Eq. (10) is not an approximation, since then the expression $\eta_{\text{det}} = 2|z_{\text{det}}|$ is exact.

D. Time dependence of electron trajectories

One of the objectives of the present work is to find explicit expressions for the photoelectron physical time t for every trajectory point and under the assumption of an electron launch at $\tau = t = 0$. From these expressions one may subsequently derive the time of flight of the electron from the ion core towards the plane of detection located at $z = z_{\text{det}}$. According to the definition of the reduced time τ , Eq. (3), the physical time $t(\tau)$ is determined as follows:

$$\begin{aligned} t(\tau) &= \int_0^\tau r(\tau') d\tau' = \frac{1}{2} \int_0^\tau (\xi(\tau') + \eta(\tau')) d\tau' \\ &= t_\xi(\tau) + t_\eta(\tau), \end{aligned} \quad (19)$$

where the second equality defines the two components $t_\xi(\tau)$ and $t_\eta(\tau)$. In order to derive general scaling laws, it is advantageous to express the integrals in terms of the scaled reduced-time variable τ_d introduced in Eq. (7). In either case, the physical time t may be obtained by calculating its components t_ξ and t_η , i.e., by integrating the analytical expressions $\xi(\tau)$ and $\eta(\tau)$ [or $\xi(\tau_d)$ and $\eta(\tau_d)$].

Hence, integration of $\xi(\tau_d)$ leads to the explicit general expression of the contribution $t_\xi(\tau_d)$ (valid for $\epsilon \geq -1$):

$$\begin{aligned} t_\xi(\tau_d) &= \frac{T_\xi}{2} \int_0^{\tau_d} \xi(\tau'_d) d\tau'_d \\ &= \frac{1}{F^{3/4}} \{ \text{dn}(y_\xi | m_\xi) (2[\epsilon^2 + \cos^2(\beta/2)]^{1/2} E(y_\xi | m_\xi) \\ &\quad - ([\epsilon^2 + \cos^2(\beta/2)]^{1/2} - \epsilon) y_\xi) \\ &\quad - ([\epsilon^2 + \cos^2(\beta/2)]^{1/2} + \epsilon) \text{cn}(y_\xi | m_\xi) \text{sn}(y_\xi | m_\xi) \}, \end{aligned} \quad (20)$$

where

$$y_\xi \equiv 2K(m_\xi)\tau_d, \quad (21)$$

$\text{dn}(x|m)$, $\text{cn}(x|m)$, and $\text{sn}(x|m)$ are the respective Jacobi elliptic functions and $E(x|m)$ the incomplete elliptic integral of the second kind [20]. Finally, the argument $m_\xi(\epsilon, \beta)$ is given in Eq. (A6) of the Appendix.

Accordingly, integration of $\eta(\tau_d)$ provides the contribution $t_\eta(\tau_d)$. In the energy range $|\epsilon| \leq \sin(\beta/2)$ (range I), this

contribution writes as

$$\begin{aligned} t_{\eta}^I(\tau_d) &= \frac{T_{\xi}}{2} \int_0^{\tau_d} \eta(\tau_d') d\tau_d' \\ &= \frac{[2 \sin(\beta/2)]^{1/2}}{F^{3/4}} \left\{ \frac{\text{sn}(y_{\eta,I}|m_{\eta}) \text{dn}(y_{\eta,I}|m_{\eta})}{1 + \text{cn}(y_{\eta,I}|m_{\eta})} \right. \\ &\quad \left. - E(\text{am}(y_{\eta,I}|m_{\eta})|m_{\eta}) + y_{\eta,I} \right\}, \end{aligned} \quad (22)$$

where

$$y_{\eta,I} \equiv 2K(m_{\eta}) \frac{\tau_d}{Q^{\infty}}, \quad (23)$$

where $\text{am}(x|m)$ is the Jacobi amplitude and $m_{\eta}(\epsilon, \beta)$ is given by Eq. (A11a).

As for the energy range *II* where $\epsilon \geq \sin(\beta/2)$, we obtain

$$\begin{aligned} t_{\eta}^{II}(\tau_d) &= \frac{2^{1/2}[\epsilon + [\epsilon^2 - \sin^2(\beta/2)]^{1/2}]^{1/2}}{F^{3/4}} \\ &\quad \times \{ \text{sc}(y_{\eta,II}|m_{\eta}) \text{dn}(y_{\eta,II}|m_{\eta}) \\ &\quad - E(\text{am}(y_{\eta,II}|m_{\eta})|m_{\eta}) \}, \end{aligned} \quad (24)$$

where

$$y_{\eta,II} \equiv K(m_{\eta}) \frac{\tau_d}{Q^{\infty}}, \quad (25)$$

with the Jacobi elliptic function $\text{sc}(x|m) = \text{sn}(x|m)/\text{cn}(x|m)$ [20] and $m_{\eta}(\epsilon, \beta)$ is now given by Eq. (A11b).

The set of Eqs. (20)–(25) is formally equivalent to Eqs. (73), (78), and (79) of Ref. [16], where they are given with a substantially different notation by Lantoine and Russell in their chapter 2.5 (precisely entitled ‘‘Stark equation,’’ though dealing with spacecraft trajectories). Nevertheless, going from their expressions to the above set of Eqs. (20)–(25) is by no means a trivial task and the present form is more convenient and suitable in the context of atomic photoionization.

IV. CALCULATION OF CLASSICAL TIMES OF FLIGHT AND TIME DELAYS

A. General evolution of the time of flight

The expressions of Eqs. (20)–(25) provide the physical time for every given point on the photoelectron trajectory. When this point is the impact point on the detector, they provide the electron’s physical source-to-detector time of flight (TOF), which is defined as

$$\text{TOF} \equiv t(\tau = T_{\eta}) = t(\tau_d = Q), \quad (26)$$

where the second equality clearly shows the connection between TOF and the parameter Q defined in Eq. (15). Explicit use of the finite detector-distance expressions for T_{η} or Q leads to finite TOFs. On the other hand, as expected, for a detector at infinity ($|z_{\text{det}}| \rightarrow \infty$, $\tau = T_{\eta}^{\infty}$, and $\tau_d = Q^{\infty}$ [see Eqs. A(12) and A(13)] the contributions $t_{\eta}^I(Q^{\infty})$ and $t_{\eta}^{II}(Q^{\infty})$ diverge, and evidently the same holds for TOF itself. Nevertheless, the relative delays between given pairs of electron trajectories remain

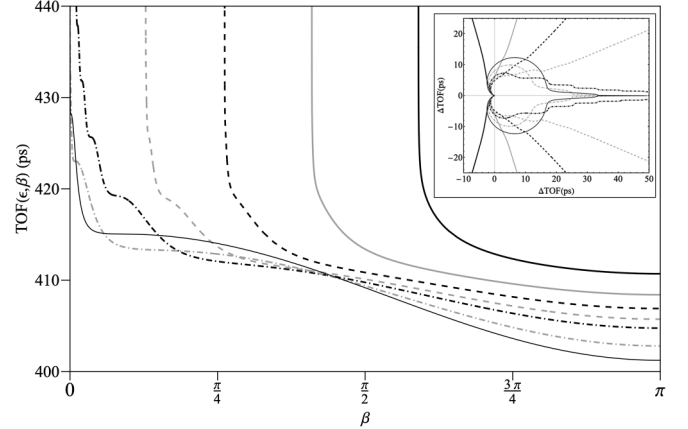


FIG. 3. Absolute electron time of flight $\text{TOF}(\epsilon, \beta)$ in photoionization in the presence of an external electric field $F = 680$ V/cm. The time of flight is evaluated at distance $|z_{\text{det}}| = 1$ mm at selected reduced-energy values within the range $\epsilon \in [-1, 1]$ as a function of the launch angle β (bold black: $\epsilon = -0.6$; dashed black: $\epsilon = -0.4$; dashed gray: $\epsilon = -0.2$; dashed-dotted black: $\epsilon = 0.0$; dashed-dotted gray: $\epsilon = 0.5$; and thin black: $\epsilon = 1.0$). The inset on the right upper part of the figure represents the difference $\Delta\text{TOF}(\epsilon, \beta) = \text{TOF}(\epsilon, \beta) - \text{TOF}(\epsilon, \pi)$ in polar form. The polar plot shows more explicitly strong oscillations, particularly visible at $\epsilon = 0$, each oscillation being related to the presence of a glory angle.

finite. However, before focusing on these relative delays it is important to first examine the general *finite* TOF evolution as a function of energy and launch angle.

Figure 3 shows calculated times of flight for different ejection angles β , at selected reduced energy ϵ values within the $[-1, 1]$ interval and for a finite but macroscopic distance $|z_{\text{det}}|$ (equal to 1 mm in the present case). The numerically computed times of flight refer to a field strength of 680 V/cm, which is among the typical field values employed in slow photoelectron imaging experiments. Nonetheless, the general shapes of the curves $\text{TOF}(F, |z_{\text{det}}|, \epsilon, \beta)$ remain the same due to their common scaling with F that is to be discussed below. These shapes exhibit a number of features that deserve to be mentioned. Note first that there are mostly two regimes in the evolution of TOF. For $\beta \rightarrow \beta_c$ (that is, $\beta \rightarrow 0$ at positive energy), TOF increases drastically and even diverges at the small-angle limit, corresponding to an electron launched in the direction opposite to the detection plane. On the other hand, when $\beta \rightarrow \pi$ the evolution of TOF is relatively flat and the time of flight tends smoothly towards its minimum value reached at $\beta = \pi$. A second feature is more visible in the inset of Fig. 3 representing the time of flight in polar coordinates. The occasionally observed strong oscillations of TOF, particularly visible at $\epsilon = 0$, relate to the glory angles. Indeed, it can be shown that the second derivative $\frac{d^2\text{TOF}}{d\beta^2}$ of the time of flight vanishes in the vicinity of the glory angles for symmetry reasons.

Further, it is interesting to compare the evolution of $\text{TOF}(F, |z_{\text{det}}|, \epsilon, \beta)$ in photoionization with the equivalent quantity $\text{TOF}_{\text{photodet}}(F, |z_{\text{det}}|, \epsilon, \beta)$ corresponding to photodetachment, that is, without the presence of any Coulomb field.

In that case the exact expression is trivial and writes as

$$\text{TOF}_{\text{photodet}}(F, |z_{\text{det}}|, \epsilon, \beta) = \frac{1}{F^{3/4}} [2\epsilon^{1/2} \cos \beta + [4\epsilon \cos^2 \beta + 2F^{1/2} |z_{\text{det}}|]^{1/2}], \quad (27)$$

where the reduced energy ϵ is introduced for a closer comparison, even though the saddle-point energy concept does not apply here. The evolution of $\text{TOF}_{\text{photodet}}$ is smooth and does not present any peculiarities compared to TOF. Equation (27), however, is quite useful for estimating the time-of-flight order of magnitude and for revealing its scaling laws with respect to the electric field. For example, at large detector distances the term containing $|z_{\text{det}}|$ dominates and represents the main contribution to the time of flight, which may be approximately expressed as

$$\text{TOF}_{\text{photodet}} \approx \left[\frac{2|z_{\text{det}}|}{F} \right]^{1/2}. \quad (28)$$

On the other hand, Eq. (27) also shows nicely that the time-of-flight difference between two trajectories corresponding to launch angles β_1 and β_2 is practically independent of $|z_{\text{det}}|$. Indeed, this difference can be simply approximated as

$$\begin{aligned} \Delta \text{TOF}_{\text{photodet}}(\epsilon, \beta_1, \beta_2) &= \text{TOF}_{\text{det}}(\epsilon, \beta_1) - \text{TOF}_{\text{det}}(\epsilon, \beta_2) \\ &\approx \frac{2\epsilon^{1/2}(\cos \beta_1 - \cos \beta_2)}{F^{3/4}}. \end{aligned} \quad (29)$$

These two essential results are also expected to be valid in photoionization. Of course, the dimensionality of all combinations $F^{-1/2} [|z_{\text{det}}|]^{1/2}$ and $F^{-3/4} \epsilon^{1/2} \propto F^{-1} E^{1/2}$ (expressed in atomic units) is physical time. Therefore, when the latter is expressed in conjunction with the dimensionless parameter ϵ , an $F^{-3/4}$ scaling law is to be expected. This can be also confirmed by simple inspection of Eqs. (20)–(25), where, apart from their $F^{-3/4}$ scaling, these physical time expressions depend on F only implicitly through ϵ .

B. Electron time delays at glory angles

The above equations allow for the connection between the reduced energy ϵ , the electron ejection angle β , the time of flight of the corresponding trajectory, and the impact radius ρ on the detector. For a given energy, each radius is reached by several trajectories corresponding to different values of β according to the number of electron oscillations along the ξ coordinate. The present work focuses on those electron trajectories that lead to $\rho = 0$ and contribute to the glory effect, thus allowing the link between classically calculated time-of-flight differences and quantum glory oscillations. Hence, at present a major part of the image is discarded. Nevertheless, much information can be already obtained by examining the information provided solely by the glory signal.

As Eq. (16) implies, there is an infinite series of glory angles $\pm \beta_k^G(\epsilon)$. However, only the lowest orders, typically with $k = 0, 1$, and 2 , contribute to the final result proportionally to the corresponding solid angle $d\Omega_k^G(\epsilon, \beta_k^G)$:

$$d\Omega_k^G(\epsilon, \beta_k^G) = 2\pi \sin \beta_k^G d\rho \left(\frac{d\rho}{d\beta} \right)_{\beta=\beta_k^G}^{-1}, \quad (30)$$

which vanishes rapidly when the integer k increases.

As mentioned above, the time of flight depends on the distance from the detector. Most of this time, however, is spent far from the Coulomb center and under the action of the dc field only. This part of the flight is more or less common to all trajectories and is not relevant here. The most natural way of obtaining time information fairly independent of $|z_{\text{det}}|$ is by defining an appropriate reference trajectory and its corresponding reference time of flight in order to calculate differences between times of flight that are more representative of an internal electronic clock. As such, here we choose as an internal reference time of flight for a given energy ϵ , the shortest one corresponding to $\beta = \pi$. Specifically, we introduce the relative time of flight at glory angles defined as

$$\begin{aligned} \Delta \text{TOF}_k^G(F, \epsilon) &\equiv \text{TOF}(F, |z_{\text{det}}|, \epsilon, \beta_k^G(\epsilon)) \\ &- \text{TOF}(F, |z_{\text{det}}|, \epsilon, \pi). \end{aligned} \quad (31)$$

Evidently, $\Delta \text{TOF}_k^G(F, \epsilon)$ corresponds to $Q = k + 1$ [Eq. (16)] and can be split into its ξ - and η components, i.e.,

$$\Delta \text{TOF}_k^G = \Delta \text{TOF}_{\xi,k}^G + \Delta \text{TOF}_{\eta,k}^G. \quad (32)$$

Given that $t_{\xi}(\epsilon, \beta = \pi) = 0$, one then finds

$$\begin{aligned} \Delta \text{TOF}_{\xi,k}^G(F, \epsilon) &= (1+k) \frac{4[\epsilon^2 + \cos^2(\beta_k^G/2)]^{1/4}}{F^{3/4}} \{E(m_{\xi,k}) \\ &- K(m_{\xi,k})(1 - m_{\xi,k})\}, \end{aligned} \quad (33)$$

where $m_{\xi,k} = m_{\xi}(\epsilon, \beta = \beta_k^G)$ [see Eq. (A6)] and $E(m)$ is the complete elliptic integral of the second kind [20]. Dealing now with the η component, and under the assumption of a detector at infinity, one first carefully separates the diverging from the nondiverging parts of $t_{\eta}(\tau_d = Q^\infty)$. It turns out that the former parts diverge irrespective of the values of the reduced energy and angle. These parts, therefore, do not contribute to any time-of-flight differences, and by applying the definition of Eq. (31) this exercise finally gives

$$\begin{aligned} \Delta \text{TOF}_{\eta,k}^G(F, \epsilon) &= \frac{2^{1/2}}{F^{3/4}} \left\{ [\sin(\beta_k^G/2)]^{1/2} [K(m_{\eta,k}) \right. \\ &- 2E(m_{\eta,k})] - \left[K\left(\frac{1-\epsilon}{2}\right) \right. \\ &\left. \left. - 2E\left(\frac{1-\epsilon}{2}\right) \right] \right\}, \end{aligned} \quad (34)$$

where $m_{\eta,k} = m_{\eta}(\epsilon, \beta = \beta_k^G)$ and where m_{η} is given exclusively by Eq. (A11a). Equations (33) and (34) are valid for $\epsilon \geq -1$, that is, for either energy range *I* or *II* [i.e., either for $|\epsilon| \leq \sin(\beta/2)$ or $\epsilon \geq \sin(\beta/2)$]. Moreover, it is important to note that contrary to Eq. (33) which is valid only for integer values of Q and thus only for the glory angles, Eq. (34) is, in fact, valid for any angle β within the $[0, \pi]$ interval.

The derivation of Eqs. (33) and (34), their analysis, and their comparison with corresponding quantum-glory computations constitute essentially the core of the present work. Furthermore, since these equations are derived for a PSD at infinity, they are free of any approximation. Nevertheless, numerical ΔTOF_k^G calculations performed for $|z_{\text{det}}| = 1$ mm and field strength of 680 V/cm show an agreement better than 0.5% with the above analytical results. Larger differences ($\sim 5\%$) are found only in the vicinity of $\epsilon \approx -1$ (for $k > 0$)

where TOF diverges (see Fig. 3). In this range, however, ΔTOF_k^G is already extremely small. It is finally verified that numerically computed ΔTOF_k^G differences do not vary with the distance between the atom and the detector as soon as $|z_{\text{det}}|$ is significantly larger than the atomic dimensions.

Figure 4(a) displays these ΔTOF_k^G curves (that is, the *time delays at glory angles*) and their components $\Delta\text{TOF}_{\xi,k}^G$ and $\Delta\text{TOF}_{\eta,k}^G$ for $k = 0, 1$, and 2 , as given by Eqs. (32), (33), and (34). The x axis is expressed in reduced energy ϵ . For the y axis we employ the scaled quantity $F^{3/4} \times \Delta\text{TOF}_k(\epsilon)$ expressed in atomic units. In view of Eqs. (20)–(25), (33), and (34), where the dependence of the physical time on the external field is entirely contained in the $F^{-3/4}$ term, this scaling results in “universal” time-delay curves, irrespective of the field value. At first glance, Fig. 4(a) shows that the components $\Delta\text{TOF}_{\xi,k}^G$ largely dominate at $\epsilon \geq 0$, yet their contribution is still important ($\sim 50\%$) at negative reduced energies larger than -0.5 . On the contrary, the components $\Delta\text{TOF}_{\eta,k}^G$ completely dominate just above the saddle-point energy, i.e., at $\epsilon \geq -1$, while at positive energies and particularly for $\epsilon \geq 0.5$ their contribution to ΔTOF_k^G does not exceed 5% . Furthermore, the components $\Delta\text{TOF}_{\xi,k}^G$ are monotonically increasing, while the components $\Delta\text{TOF}_{\eta,k}^G$ exhibit a maximum which shifts towards $\epsilon = -1$ as k increases. These quite different functional forms and energy ranges of dominance between the two delay components create two distinct regimes of delay evolution, depending on whether the energy is negative or positive. In the former case, $\epsilon < 0$, the evolution of delays ΔTOF_k^G differs significantly according to the order k . Notice in particular the quasiplateau over a large fraction of the negative energy region for $k = 2$. Consequently, there is no obvious link among the delay curves for different k .

On the contrary, for $\epsilon \geq 0$ the delays ΔTOF_k^G increase monotonically due to the dominance of $\Delta\text{TOF}_{\xi,k}^G$ in this energy range. For the sake of comparison, Fig. 4(a) also includes the corresponding quantity in photodetachment (where there is no glory effect) that describes the time-of-flight difference between the two trajectories leading to $\rho = 0$. This curve is given by Eq. (29), namely, $F^{3/4} \Delta\text{TOF}_{\text{photodet}}(\epsilon, \beta_1 = 0, \beta_2 = \pi) = 4 \epsilon^{1/2}$, and we can observe that it almost matches $\Delta\text{TOF}_{k=0}^G(\epsilon)$ at large positive ϵ values. In fact, the proportionality of ΔTOF to $\epsilon^{1/2}$ in the $\epsilon \rightarrow \infty$ limit [that, in fact, can be relaxed to the $\epsilon \gg |\cos(\beta_k^G/2)|$ condition] is to be expected also for $\Delta\text{TOF}_{\xi,k}^G$ and consequently ΔTOF_k^G , since then $m_{\xi,k} \rightarrow 1$, $E(m_{\xi,k}) \rightarrow 1$, $K(m_{\xi,k})(1 - m_{\xi,k}) \rightarrow 0$, and Eq. (33) predicts $F^{3/4} \Delta\text{TOF}_{\xi,k}^G \approx 4(1+k)\epsilon^{1/2}$. This result implies that the contributions $\Delta\text{TOF}_{\xi,k}^G$ should be proportional to each other in the $\epsilon \gg |\cos(\beta_k^G/2)|$ limit. We examine this statement in Fig. 4(b), which shows the $F^{3/4} \Delta\text{TOF}_{\xi,k}^G$ components divided by $Q = k + 1$. The practically exact matching between the $k = 1$ and $k = 2$ curves over the full $-1 \leq \epsilon \leq 2$ interval is striking. The $k = 0$ curve also matches exactly the other two at positive energies, differing in the negative-energy part due to its different appearance threshold [see Eq. (18)]. Thus, the proportionality among $\Delta\text{TOF}_{\xi,k}^G$ curves approximately holds for every energy $\epsilon \geq -1$. However, at positive energies ΔTOF_k^G is practically identical to $\Delta\text{TOF}_{\xi,k}^G$ and Fig. 4(b) unambiguously shows that all glory delays are almost

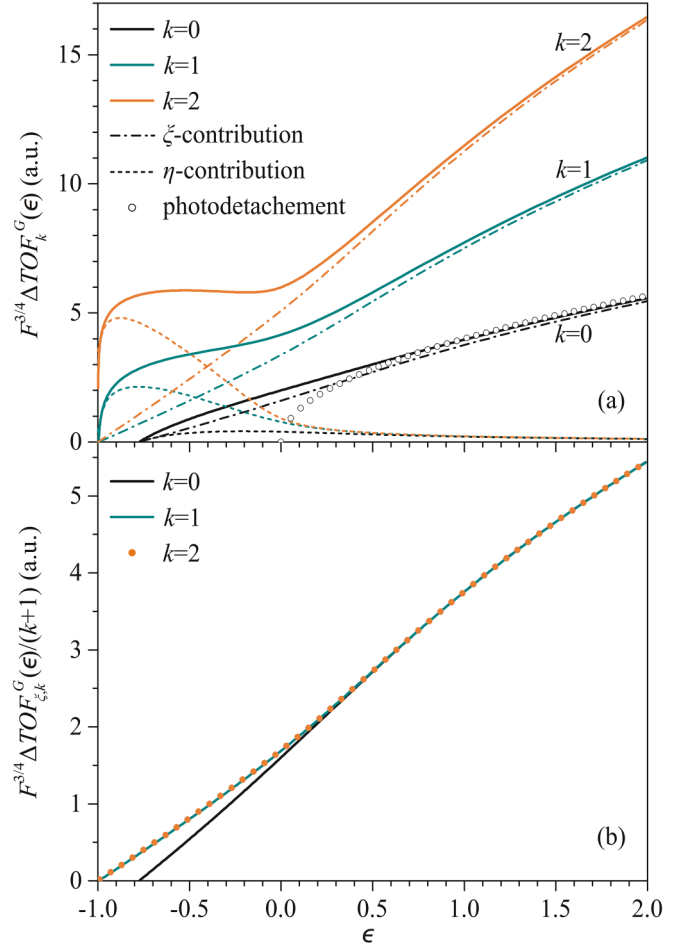


FIG. 4. (a) Reduced energy dependence of the field-scaled differences between the photoelectron time of flight of the trajectory corresponding to glory angle $\beta_k^G(\epsilon)$ and the trajectory of shortest time of flight at angle $\beta = \pi$. The angles $\beta_k^G(\epsilon)$ are obtained by solving Eq. (16) for each glory order $Q = k + 1$, with $k = 0$ (black), 1 (cyan), and 2 (orange). These scaled photoionization time delays, $F^{3/4} \Delta\text{TOF}_k^G(\epsilon)$ (full lines), are defined in Eq. (31) and they are split into their ξ - and η contributions [see Eqs. (32)–(34)], which are drawn in the graph with dashed-dotted and dashed lines, respectively. Equations (33) and (34) assume the detector is placed at infinity. In general, the time delays are independent of the atom-to-detector distance as soon as $|z_{\text{det}}|$ is significantly larger than the atomic dimensions. Then, Eqs. (33) and (34) practically cover the finite $|z_{\text{det}}|$ distance case as well. (b) Field-scaling, accomplished by multiplying the time-delay curves by $F^{3/4}$, ensures these curves are valid whatever the field strength. For comparison, the equivalent quantity in the case of photodetachment, $F^{3/4} \Delta\text{TOF}_{\text{photodet}}(\epsilon, \beta_1 = 0, \beta_2 = \pi) = 4 \epsilon^{1/2}$ [see Eq. (29)], is also plotted for $\epsilon \geq 0$ with white circles. (b) Field-scaled ξ contributions [Eq. (33)] divided by the glory order $k + 1$. For $\epsilon > 0$ the curves are practically indistinguishable, thus signaling the mutual proportionality between the undivided $F^{3/4} \Delta\text{TOF}_{\xi,k}^G(\epsilon)$ curves given in (a).

proportional to the shortest delay according to $\Delta\text{TOF}_k^G(\epsilon) \approx (k + 1) \times \Delta\text{TOF}_{k=0}^G(\epsilon)$.

Having derived and analyzed the classical time delays at glory angles and different orders k , the remaining task of this work is to link these delays with the corresponding

quantum-mechanical predictions of the glory effect. In particular, the time-delay curves need to be connected to the complexity of the computed (as well as to the experimentally observed) so-called glory spectra, that is, the variation of the signal at the center of the images as a function of excitation energy. This connection entails implications related to the quantum-classical correspondence and it will be examined in the next section.

V. COMPARISON WITH QUANTUM CALCULATIONS: TIME DELAYS AND SPECTRAL FEATURES

A. General considerations on quantum-classical correspondence

The formal correspondence and link between the classical frequency of motion and the transition frequency between successive quantum states is a universal property of microsystems. For example, in atomic physics we find the equivalence between the perfectly periodic revolution period of a Rydberg electron and the energy gap between successive Rydberg levels. Similar examples concern molecular vibration and rotation and it is commonly believed that this correspondence holds almost exclusively for periodic or quasiperiodic motion.

Clearly, the problem examined in the preceding sections of the present work deals with nonperiodic electron motion: each glory order, $(k + 1)$, corresponds to an extremely limited number of quasirevolutions around the core [typically $\sim (k + 1)/2$] before the electron ionizes. Under these conditions one would not expect to find any signature of the classical timing information associated with electronic motion in the corresponding spectral structures. And yet, on the contrary, not only does this correspondence exist, but it is also very robust and allows, at least in the region of positive energies, to extract from the spectral data quite precise values of the time delays at glory angles. This will be demonstrated by comparing the classical time delays $\Delta\text{TOF}_k^G(\epsilon)$ provided above with time information extracted from a hydrogenic glory spectrum calculated in the framework of a quantum model described in Ref. [1]. In fact, rather than analyzing the detailed structure of the glory spectrum, we are interested in extracting global information from it. As compared to the experimental data [5], the present comparison has the advantage of benefiting from the arbitrarily high resolution and the superior signal-to-noise ratio of the calculation. This additionally allows identifying precisely features of classical or purely quantum origin.

B. Glory interference spectroscopy and its connection to classical time delays at glory angles

The idea that interference phenomena exhibited by the photoelectron momentum distribution $R(\epsilon, \rho)$ may, under certain conditions, provide information on the ionization time delays between classes of electron trajectories, was already suggested in Ref. [21]. Here, the focus is on the spectral characteristics of the glory signal $R(\epsilon, \rho = 0)$. To demonstrate this, we employ the quantum-mechanical theory of the Stark effect for the hydrogen atom. What is initially calculated is the outgoing flux of electrons released by photoionization in the presence of the static field, or, in other words, the probability

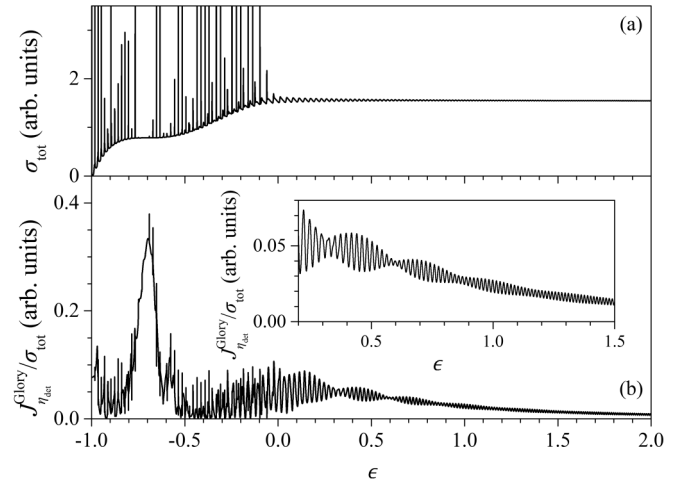


FIG. 5. Single-photon ionization of hydrogen atom out of its ground state and under the presence of an external electric field $F = 680$ V/cm. The linear laser polarization is parallel to the field axis, resulting in the exclusive excitation of $m = 0$ final Stark states. (a) Total ionization cross section σ_{tot} as a function of reduced energy ϵ . (b) Glory signal divided by σ_{tot} as a function of reduced energy (the *scaled* glory spectrum). Scaling minimizes the presence of the sharp and intense resonances that belong to long-lived quasibound Stark states and they are observed in (a) for $\epsilon < 0$. The inset shows the $\epsilon > 0$ part of the scaled glory spectrum in more detail.

current density,

$$J_{\eta_{\text{det}}}(\xi, \phi) = i\pi\alpha\omega (\xi + \eta)^{-1/2} \times \left[\psi \left(\frac{\partial \psi^*}{\partial \eta} \right) - \psi^* \left(\frac{\partial \psi}{\partial \eta} \right) \right] \Big|_{\eta=\eta_{\text{det}}}, \quad (35)$$

along a paraboloid of constant η_{det} . In the above equation α is the fine-structure constant and ω the frequency of the photoionizing laser field, whose intensity is incorporated in the terms involving the wave function ψ . In fact, when $\eta_{\text{det}} \rightarrow \infty$ this paraboloid coincides with the detection plane at z_{det} . Note that $J_{\eta_{\text{det}}}$ depends on the dipole transition matrix elements involved in the excitation and ionization process [1,5,22]. In the present work we deal with single-photon excitation of the final Stark states of hydrogen atom out of its $m = 0$ ground state. The linear polarization of the ionizing radiation is assumed parallel to the dc-field axis. The relevant $\Delta m = 0$ dipole selection rule leads to the excitation of $m = 0$ final Stark states only. Then, the resulting images show no angular dependence and $R(\epsilon, \rho) = 2\pi J_{\eta_{\text{det}}}$. Other polarization settings and $m \neq 0$ final states are not examined, since, in agreement with the classical calculation, it turns out that only $m = 0$ states contribute to the glory signal $J_{\eta_{\text{det}}}^{\text{glory}} \equiv J_{\eta_{\text{det}}}(\rho = \xi = 0, \phi)$ at the center of $J_{\eta_{\text{det}}}(\xi, \phi)$ [5]. Details about the computation are given in Ref. [1], where the alternative $(\chi = \xi^{1/2}, \nu = \eta^{1/2}, \varphi)$ parabolic coordinate system [16] was used.

By integrating $J_{\eta_{\text{det}}}$ over the whole detector surface one finds the total ionization cross section σ_{tot} . Figure 5(a) displays the calculated hydrogenic σ_{tot} as a function of reduced energy and for the field strength $F = 680$ V/cm that corresponds to the value employed experimentally in

Ref. [5]. For $\epsilon > 0$, σ_{tot} exhibits an oscillatory behavior. The periodicity of the observed structures increases, and their amplitude diminishes as energy increases [23–25]. Nowadays they are attributed to the, so-called, static field-induced states [26] which, as their widths imply, are relatively short-lived. On the contrary, for $\epsilon < 0$, σ_{tot} is dominated by sharp and very intense resonances which are built upon a smoothly varying background. Their sharpness necessitated the use of an extremely dense reduced-energy grid with a constant step of $\delta\epsilon = 5 \times 10^{-5}$ over the full $-1 \leq \epsilon \leq 2$ range. These resonances are also visible in the glory spectrum and belong to long-lived, quasibound states where the electron escapes solely via tunneling. They are not, therefore, relevant within a classical description. For this reason, the glory signal is divided by σ_{tot} , and the resulting *scaled* glory spectrum is shown in Fig 5(b). In fact, the division by σ_{tot} was first employed experimentally [1,5] in order to minimize systematic errors stemming from fluctuations in the experimental signal. Obviously, the division greatly reduces the importance of resonances in the $\epsilon < 0$ region. On the other hand, for $\epsilon > 0$ the aforementioned ionization cross section oscillations have similar frequency structure with the glory oscillations but they probe quite different phenomena [5,25,26]. In addition, the division of the glory spectrum by σ_{tot} appears to have a negligible effect in the positive-energy range, due to the quite small contrast of the cross section oscillations (resulting in a quasiconstant magnitude of σ_{tot}).

The gross features exhibited by the calculated scaled glory spectrum of Fig. 5(b) can be summarized as follows: (i) The negative-energy spectral structures are complex, and their evolution is irregular. There is a dominant broad structure around $\epsilon \approx -0.65$ and a much weaker one at $\epsilon \approx -1$, both being of classical origin [3]. Noteworthy is the absence of high-frequency oscillations on the former broad structure, as compared to its red and blue side. This observation, however, cannot be generalized. (ii) The positive-energy spectrum exhibits quasiregular oscillations at high frequency which are modulated by lower-frequency beatings. A quasiperiodic structuring of the $\epsilon > 0$ glory spectrum is thus quite obvious, clearly indicating that the spectrum contains temporal information. Furthermore, it is verified that this spectrum is not dominated by a characteristic “single-frequency” periodicity, but, rather, exhibits a periodicity that gradually increases with energy. Hence, the so-called “short-time Fourier transform” (STFT) appears as the most appropriate technique for extracting this temporal information. The method is usually employed for determining the varying frequency and phase content of local fractions of a time-varying signal [27]. In short, a selected window function is continuously dragged along the energy axis and the Fourier transform is applied only in the interval covered by the window. In our case, the result of such a transformation of a one-dimensional spectrum is a two-dimensional (2D) representation of the spectral frequency content as a function of (reduced) energy. Among the different windowing possibilities, we also found it more suitable to choose a Blackman window function [28]. Finally a smooth STFT distribution is achieved by setting the overlap between successive energy windows to be as large as possible, i.e., comparable to the window width.

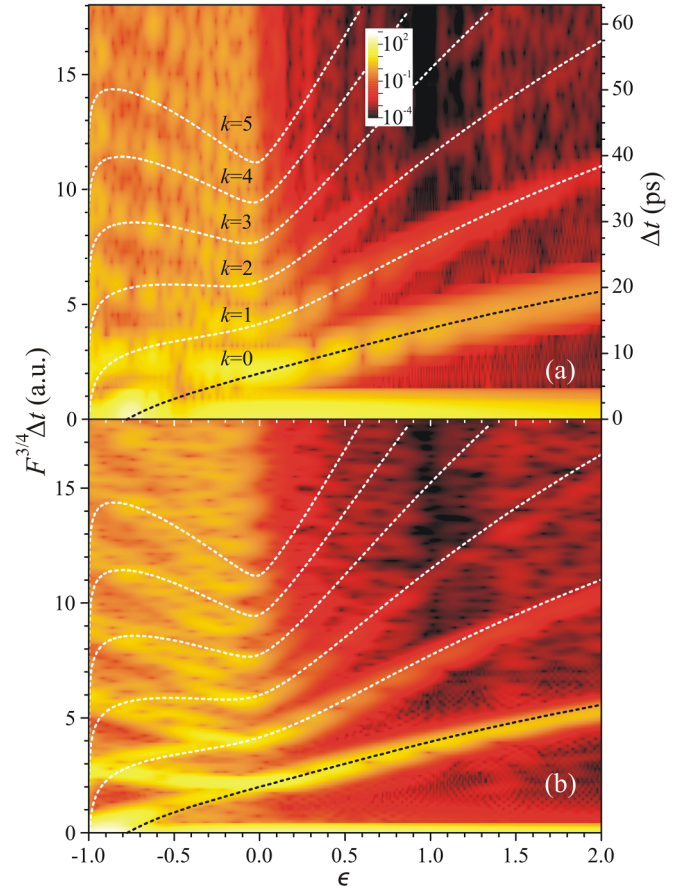


FIG. 6. Short-time Fourier transform (STFT) maps of the scaled glory spectrum of Fig. 5(b), calculated for two different reduced-energy windows w_ϵ , namely $w_\epsilon \approx 0.13$ (a) and $w_\epsilon \approx 0.41$ (b). In both plots the overlap between successive windows is comparable to each w_ϵ . The left y axis is expressed in atomic units of the scaled quantity $F^{3/4} \times \Delta t$, and the above reduced-energy windows lead to its uncertainties of ≈ 0.46 a.u. in (a) and of ≈ 0.15 a.u. in (b). The right y axis is expressed in time units picoseconds (ps) for the specific electric field strength $F = 680$ V/cm employed for the calculations presented in Fig. 5. The inset of (a) shows the [common in (a) and (b)] logarithmic color scale, which covers 7 orders of magnitude. Superimposed in both STFT maps are the scaled classical time delays $F^{3/4} \times \Delta \text{TOF}_k^G(\epsilon)$ [Eqs. (32)–(34)], with $k = 0$ (black dashed line) and $k = 1 - 5$ (white dashed lines).

Two-dimensional STFT maps derived from the computed, scaled hydrogenic glory signal of Fig. 5(b) are displayed in Figs. 6(a) and 6(b), where we obviously deal with the usual frequency- (energy)-time pair, but with this pair interchanged in the x - and y axes. The x axis is given in terms of reduced energy ϵ . For the (left) y axis we again employ the scaled quantity $F^{3/4} \times \Delta t$ expressed in atomic units, where Δt refers to time differences. To get a feeling of the actual magnitude of these time delays, the right y axis of the graph of Fig. 6(a) is expressed in time units (ps) for the specific external electric field value of $F = 680$ V/cm. Apart from the scaling, however, it is important to remember that the details of the produced 2D STFT representation are sensitive to the width

of the employed energy window. For the above field strength used in Ref. [5] we calculate $E_{\text{sp}} = -159.6 \text{ cm}^{-1}$. In that work it was found that for $\epsilon > 0$ a reasonable compromise between frequency and temporal resolution would be an energy window length of about 21 cm^{-1} that allows for a temporal uncertainty of $\approx 1.6 \text{ ps}$. Transformed to the energy- and time quantities employed here, the above choice corresponds to a reduced-energy window $w_\epsilon \approx 0.13$ and an uncertainty of $\approx 0.46 \text{ a.u.}$ for the scaled time difference $F^{3/4} \times \Delta t$. The present STFT map under these conditions is given in Fig. 6(a). While it appears adequate for the positive-energy range, it results, however, in somewhat blurred 2D structures on the $\epsilon < 0$ side, where many fine details are lost. Therefore, for obtaining a clearer visualization of these negative-energy structures, the plot shown in Fig. 6(b) is constructed with a window $w_\epsilon \approx 0.41$, leading to an uncertainty of $\approx 0.15 \text{ a.u.}$ for the quantity $F^{3/4} \times \Delta t$. Going back to the field strength of 680 V/cm , the energy window is now $\approx 65 \text{ cm}^{-1}$ (about three times larger with respect to the one employed in Ref. [5]), leading to a time uncertainty of $\approx 0.5 \text{ ps}$. Below, we discuss in some detail the so-obtained STFTs over the full $-1 \leq \epsilon \leq 2$ range, using on each occasion the most appropriate graph of Fig. 6.

Each of the 2D maps of Fig. 6 can be interpreted as a power spectrum since it displays the weight of any given scaled time component at a definite value of the reduced energy, both quantities subjected to the above-mentioned respective uncertainties. Clearly, for either Fig. 6(a) or 6(b), the situation between the negative- and positive-energy ranges is highly contrasted. Common in both ranges and graphs is a horizontal branch close to $\Delta t \approx 0$ that corresponds to the dc Fourier component at each window energy location. It reflects the “envelope” of the glory spectrum, i.e. its average over the window length as a function of reduced energy. Let us first note that the y -axis width of this branch for each plot is wider than the aforementioned corresponding uncertainty of $F^{3/4} \times \Delta t$. Furthermore, it is interesting to compare this envelope with the universal classical scaled glory curves [3] (see Fig. 11 therein). Such a comparison shows that the envelope additionally reflects phenomena of quantum origin, e.g., the gross beating and signal cancellation behavior of the glory spectra seen in Fig. 5(b) around $\epsilon \approx -0.5$. This cancellation has no classical counterpart.

Apart from this branch, the positive-energy power spectrum reveals a strong time-frequency structuring into several (essentially three) branches that increase monotonically with ϵ . This fairly simple branch picture is obviously correlated with the rather regular structure of the glory spectrum in this energy range. One may remark first that in general, the highest the slope the faintest the branches, thus necessitating the employment of a logarithmic color scale covering 7 orders of magnitude. The meaning of these branches becomes evident if one compares them with the classical scaled time delays $F^{3/4} \times \Delta\text{TOF}_k^G(\epsilon)$, $k = 0 - 2$ of Fig. 4(a), which are superimposed on both maps of Fig. 6. Comparing first with the map of Fig. 6(a), we note that as expected [5], the classical curves perfectly pass within the scaled-time width of the quantum-mechanically computed hydrogenic glory STFT branches. Nevertheless, a comparison with the map of Fig. 6(b) shows

that the classical curves still follow quite faithfully the corresponding STFT branches, even though at the highest ($\epsilon > 1$) reduced-energy range they marginally fail to pass within the (much smaller) scaled-time widths of these branches. Thus, the observed discrepancies (that worsen as k increases) are acceptable and of the order of these widths. Furthermore, even under these conditions the STFT branches nicely reproduce the $F^{3/4}\epsilon^{1/2}$ scaling exhibited by the classical curves at the large positive reduced-energy limit. Therefore, the agreement between classical and quantum results in Fig. 6(b) can be characterized as very good. From a qualitative point of view, this agreement confirms the intimate link between glory oscillations and characteristic travel times along classical glory trajectories. As it is mentioned above, for $\epsilon > 0$ it holds that $\Delta\text{TOF}_k^G(\epsilon) \approx (k+1) \times \Delta\text{TOF}_{k=0}^G(\epsilon)$ (see also Fig. 4). Therefore, the main high “carrier” oscillation periodicity of the glory signal is directly related to this characteristic time, with a spectral distance between successive peaks given roughly by $(\Delta\text{TOF}_{k=0}^G(\epsilon))^{-1}$. On the other hand, the beating pattern observed at lower spectral frequencies is itself directly related to the difference between these characteristic time differences, with the spacing between nodes roughly proportional to the inverse of these differences. This explicit link can be quantified in a rigorous semiclassical approach that will be developed in a separate paper.

Let us finally focus on the negative-energy part of the power spectrum. The above discussion pointed out the role of the reduced-energy window w_ϵ . The latter is nothing more than an adjustable analysis parameter, an image-processing tool, making at least some of the details of the STFT map structures sharper, while keeping in mind at the same time that the computed glory spectrum as well as the classical time-delay curves do not actually depend on any adjustable parameter. As it becomes evident by visual inspection, the conditions employed for creating the graph of Fig. 6(b) are more appropriate for $\epsilon < 0$. They result in an STFT map which is highly structured, thus reflecting the complexity of the scaled glory spectrum in this range. Particularly, a series of closely spaced and fairly isolated “harmonics” is observed near $\epsilon \approx -1$. These branches are monotonically decreasing up to $\epsilon \approx 0$, where they exhibit a local minimum before they evolve to the above-discussed positive-energy ones. In contrast to their positive-energy counterparts that fade away as k increases, these branches have high and approximately identical intensity at all orders. The classical $\Delta\text{TOF}_k^G(\epsilon)$ curves with $k > 2$ shown in Fig. 6 reproduce indeed the $\epsilon < 0$ monotonic decrease and the minima of the branches (caused by the dominance of their $\Delta\text{TOF}_{n,k}^G$ parts). Apart, however, from these gross features the agreement between classical and quantum results is not as good as for the positive energies, particularly for low $k \leq 2$. Furthermore, the situation becomes even more complicated by the presence of additional branches interconnecting the harmonics within this $-1 \leq \epsilon < 0$ range. These structures are therefore not connected to ΔTOF_k^G curves, but it is unlikely to be related to quasibound states, since the latter play only a minimal role in the scaled glory spectra. Hence, here we deal again with the continua, and it is quite probable that at least part of this information is of classical origin. Note that as opposed to the $\epsilon > 0$ case, the $-1 \leq \epsilon < 0$ range is

characterized by a large number of glory angles of appreciable magnitude (see Fig. 2). Then, we may speculate that these additional branches stem from more complicated glory-beating terms. Stating in another, more qualitative way, the more complex situation observed in this range, as compared to the $\epsilon > 0$ one, should stem from characteristic times that are distinctly different and no longer multiples of one another. This would explain the irregularity of glory oscillations and the beating patterns observed on a larger energy scale. This range therefore requires further investigation, particularly when examining nonhydrogenic atoms where the finite size of the ionic core is expected to introduce additional difficulties.

VI. CONCLUSION

We have presented the detailed calculation of classical times of flight of electron trajectories, specifically within the context of photoionization under the presence of a dc electric field. The study has led particularly to the derivation of analytical formulas providing time delays between the trajectories contributing to the glory signal. These formulas, evaluated with the numerically calculated ejection angles of the glory trajectories, have been compared with the Fourier content of the glory signal obtained by a complete hydrogenic quantum model. It has been shown that by applying a simple short-time Fourier transform procedure to the strong quasiperiodic oscillations and beating patterns exhibited by the quantum glory signal in the positive-energy range, the classical time-delay curves may be recovered.

The above connection between classical time delays and glory-specific spectral features constitutes one of the most striking aspects of the present work. It vividly illustrates the principle of correspondence and the close link between the temporal characteristics of the classical motion and the energy differences between neighboring quantum spectral structures. Particularly, our results extend the application of the principle to the ionization continuum. Therefore, lying at the core of this work, this correspondence is generalized to the nonperiodic classical motion, in connection with the energy differences between successive maxima of the glory oscillations.

The agreement between classical time delays and the Fourier content of the glory signal in the negative-energy range is not as good as in the positive one, but still fairly acceptable. Undoubtedly, the negative-energy range needs further examination for the remaining discrepancies to be understood and resolved. Additional complications are to be expected when these studies are extended to nonhydrogenic atoms. The challenge here is to extract the nonhydrogenic part of the photoemission time delay and compare it with a complete quantum modeling of the Stark effect, taking into account the nonzero quantum defects of the atomic Rydberg states involved.

Furthermore, these types of (classical and quantum) studies need to cover the whole map of transverse photoelectron momentum [1], which is to be extended to nonzero radii of impact $\rho > 0$, as compared to the $\rho = 0$ radius corresponding to the glory signal. The extraction of classical time delays from a hydrogenic $\rho > 0$ zone and over a small energy range was already performed earlier [21]. It was initially expected to

provide access to photoemission time delays over the picosecond and femtoscale timescales (for the applied dc-field strengths < 1 kV/cm). In fact, the agreement between experiment and theory was not satisfactory when different radii points of the transverse photoelectron momentum map were involved, these points being related to the shortest timescales. Hence, the subject is indeed still open to investigation.

It is finally suitable to comment upon the apparent association of the present dc-field study (where the explicit temporal resolution of the dynamics is still lacking) with aspects of strong, ac-laser field physics and attosecond science. In fact, it is by now well established that glory (re-)scattering is an essential ingredient for explaining the quantum interference patterns in strong-field photoelectron holography and the low-energy structures observed in strong-field atomic ionization [29]. Furthermore, interesting associations [5] can be envisioned with the study of photoemission delays [30] in the field of ultrafast processes. From a purely intuitive point of view, it is evident that there is a deep connection between the physics described here and the study of photoionization delays. Nevertheless, the steps to be taken in order to clearly associate the ultimate temporal resolution and our direct observations of the quantum properties of the outgoing electron current, remain a qualitative challenge. This will be one of our main objectives in the near future.

APPENDIX

The classical problem of the electron motion under the combined action of an attractive Coulomb center and a homogeneous static electric field is fully integrable. Following Refs. [6,10,11] the equations of motion for total electron energy E (with $E = 0$ denoting the ionization threshold in the absence of the external electric field) are separable in parabolic coordinates as follows (in atomic units),

$$\begin{aligned} \frac{d\xi}{d\tau} &= 2\xi \left[\frac{1}{2}E + \frac{Z_1}{\xi} - \frac{p_\phi^2}{4\xi^2} - \frac{1}{4}F\xi \right]^{1/2} \\ \frac{d\eta}{d\tau} &= 2\eta \left[\frac{1}{2}E + \frac{Z_2}{\eta} - \frac{p_\phi^2}{4\eta^2} + \frac{1}{4}F\eta \right]^{1/2} \\ \dot{\phi} &= \frac{1}{\xi\eta} p_\phi, \end{aligned} \quad (\text{A1})$$

where the separation constants Z_1 and Z_2 are related by $Z_1 + Z_2 = Z$, with Z the atomic charge of the ion core ($Z = 1$ in the present case). The momentum p_ϕ along coordinate ϕ , that is, the projection of the orbital angular momentum on the field axis, is a constant of motion. The presently examined planar motion corresponds to $p_\phi = 0$, resulting in $\phi = \phi_0 = \text{constant}$. Then, it is easy to show that starting at the origin ($\xi_0 = \eta_0 = 0$), the separation constants are related to the ejection angle β with respect to the field axis ($0 \leq \beta \leq \pi$) according to

$$\begin{aligned} Z_1 &= \cos^2(\beta/2) \\ Z_2 &= \sin^2(\beta/2). \end{aligned} \quad (\text{A2})$$

Integration of Eq. (A1) [11] provides the parabolic coordinates ξ and η of the electron, as a function of the reduced-time

variable τ [Eq. (3)] and in terms of the cosine and sine Jacobi elliptic functions $\text{cn}(x|m)$ and $\text{sn}(x|m)$. Above the saddle-point energy ($E \geq E_{\text{sp}}$, $\epsilon \geq -1$), i.e. the continuum energy range, the expression of the motion along the ξ coordinate writes as

$$\xi(\tau) = \frac{\xi_+ \text{sn}^2(\varphi(\tau)|m_\xi)}{m_\xi^{-1} - \text{sn}^2(\varphi(\tau)|m_\xi)}, \quad (\text{A3})$$

with

$$\xi_+ = \frac{2([\epsilon^2 + \cos^2(\beta/2)]^{1/2} - \epsilon)}{F^{1/2}}. \quad (\text{A4})$$

The variable and argument of the elliptic sine Jacobi function are defined, respectively, as

$$\varphi(\tau) = F^{1/4}[\epsilon^2 + \cos^2(\beta/2)]^{1/4} \tau \quad (\text{A5})$$

and

$$m_\xi = \frac{1}{2} \left(1 + \frac{\epsilon}{[\epsilon^2 + \cos^2(\beta/2)]^{1/2}} \right). \quad (\text{A6})$$

Whatever the energy, the motion of the electron along parabolic coordinate ξ is periodic in τ , with a period T_ξ defined as

$$T_\xi = \frac{1}{F^{1/4}} \frac{2K(m_\xi)}{[\epsilon^2 + \cos^2(\beta/2)]^{1/4}}, \quad (\text{A7})$$

where $K(m)$ is the complete elliptic integral of the first kind [20]. The parabolic coordinate ξ is zero whenever $\tau = (k+1)T_\xi$, with k a non-negative integer.

For the motion along the η coordinate, we remind that within the continuum energy range $0 \geq \epsilon \geq -1$ there exists a critical angle $\beta_c \equiv 2 \arcsin |\epsilon|$ below which the classical motion along η is bound and ionization is classically forbidden. For $\epsilon \geq 0$, $\beta_c = 0$. For $\epsilon \geq -1$ and within the interval $\beta_c \leq \beta \leq \pi$, the electron motion along the η coordinate is given by

$$\eta(\tau) = \begin{cases} \eta_+ \left(\frac{1 - \text{cn}(\Theta(\tau)|m_\eta)}{\text{sn}(\Theta(\tau)|m_\eta)} \right)^2 & \text{for } |\epsilon| \leq \sin(\beta/2) \\ \eta_+ \frac{\text{sn}^2(\Theta(\tau)|m_\eta)}{1 - \text{sn}^2(\Theta(\tau)|m_\eta)} & \text{for } \epsilon \geq \sin(\beta/2) \end{cases} \quad (\text{A8a})$$

$$\eta_+ = \begin{cases} \frac{2}{F^{1/2}} \sin(\beta/2) & \text{for } |\epsilon| \leq \sin(\beta/2) \\ \frac{2}{F^{1/2}} (\epsilon - [\epsilon^2 - \sin^2(\beta/2)]^{1/2}) & \text{for } \epsilon \geq \sin(\beta/2) \end{cases} \quad (\text{A9a})$$

where the amplitude η_+ is written as

$$\eta_+ = \begin{cases} \frac{2}{F^{1/2}} \sin(\beta/2) & \text{for } |\epsilon| \leq \sin(\beta/2) \\ \frac{2}{F^{1/2}} (\epsilon - [\epsilon^2 - \sin^2(\beta/2)]^{1/2}) & \text{for } \epsilon \geq \sin(\beta/2) \end{cases} \quad (\text{A9b})$$

while the variable and argument of the elliptic functions are defined, respectively, as

$$\Theta(\tau) = \begin{cases} F^{1/4} [4\sin^2(\beta/2)]^{1/4} \tau & \text{for } |\epsilon| \leq \sin(\beta/2) \\ \frac{F^{1/4}}{2^{1/2}} [\epsilon + [\epsilon^2 - \sin^2(\beta/2)]^{1/2}]^{1/2} \tau & \text{for } \epsilon \geq \sin(\beta/2) \end{cases} \quad (\text{A10a})$$

and

$$m_\eta = \begin{cases} m_\eta^I = \frac{1}{2} \left(1 - \frac{\epsilon}{\sin(\beta/2)} \right) & \text{for } |\epsilon| \leq \sin(\beta/2) \\ m_\eta^{II} = \frac{2}{\left(1 + \frac{\epsilon}{[\epsilon^2 - \sin^2(\beta/2)]^{1/2}} \right)} & \text{for } \epsilon \geq \sin(\beta/2) \end{cases} \quad (\text{A11a})$$

$$m_\eta = \begin{cases} m_\eta^I = \frac{1}{2} \left(1 - \frac{\epsilon}{\sin(\beta/2)} \right) & \text{for } |\epsilon| \leq \sin(\beta/2) \\ m_\eta^{II} = \frac{2}{\left(1 + \frac{\epsilon}{[\epsilon^2 - \sin^2(\beta/2)]^{1/2}} \right)} & \text{for } \epsilon \geq \sin(\beta/2) \end{cases} \quad (\text{A11b})$$

By inspection, the electron escapes to infinity as soon as the denominator in Eqs. (A8a) or (A8b) above is zero. This corresponds to $\tau = T_\eta^\infty$, the latter given in Eq. (13) and reproduced below:

$$T_\eta^\infty = \frac{2K(m_\eta^I)}{[4\sin^2(\beta/2)]^{1/4}}. \quad (\text{A12})$$

Equation (A12) holds for any $\epsilon \geq -1$ and with m_η^I given from (A11a).

Finally, the number of periods along the ξ coordinate corresponding to the electron escape to infinity is given by the ratio $Q(\epsilon, \beta)$ defined in Eq. (15). For a detector at infinity, it writes as

$$Q^\infty \equiv \frac{T_\eta^\infty}{\tau_\xi} = \frac{K(m_\eta^I)}{K(m_\xi)} \left[\frac{\epsilon^2 + \cos^2(\beta/2)}{4\sin^2(\beta/2)} \right]^{1/4} \quad (\text{A13})$$

for any $\epsilon \geq -1$ and, again, with m_η^I given from (A11a).

- [1] P. Kalaitzis, S. Danakas, F. Lépine, C. Bordas, and S. Cohen, *Phys. Rev. A* **97**, 053412 (2018).
- [2] H. M. Nussenzveig, *Diffraction Effects in Semiclassical Scattering* (Cambridge University Press, Cambridge, 1992).
- [3] S. Cohen, P. Kalaitzis, S. Danakas, F. Lépine, and C. Bordas, *J. Phys. B* **50**, 065002 (2017).
- [4] C. Nicole, H. L. Offerhaus, M. J. J. Vrakking, F. Lépine, and C. Bordas, *Phys. Rev. Lett.* **88**, 133001 (2002).
- [5] P. Kalaitzis, S. Danakas, K. Ferentinou, F. Lépine, C. Bordas, and S. Cohen, *Phys. Rev. A* **102**, 033101 (2020).
- [6] Yu. N. Demkov, V. D. Kondratovich, and V. N. Ostrovskii, *JETP Lett.* **34**, 403 (1981).
- [7] A. T. J. B. Eppink and D. H. Parker, *Rev. Sci. Instrum.* **68**, 3477 (1997).
- [8] H. L. Offerhaus, C. Nicole, F. Lépine, C. Bordas, F. Rosca-Pruna, and M. J. J. Vrakking, *Rev. Sci. Instrum.* **72**, 3245 (2001).
- [9] P. Kalaitzis, S. Danakas, C. Bordas, and S. Cohen, *Phys. Rev. A* **99**, 023428 (2019).
- [10] V. V. Beletzky, *Essays on the Motion of Celestial Bodies* (Mir, Moscow, 1977).
- [11] V. D. Kondratovich and V. N. Ostrovsky, *J. Phys. B: At. Mol. Phys.* **17**, 2011 (1984).
- [12] C. Bordas, *Phys. Rev. A* **58**, 400 (1998).
- [13] C. Nicole, I. Sluimer, F. Rosca-Pruna, M. Warntjes, M. Vrakking, C. Bordas, F. Texier, and F. Robicheaux, *Phys. Rev. Lett.* **85**, 4024 (2000).
- [14] C. Bordas, F. Lépine, C. Nicole, and M. J. J. Vrakking, *Phys. Rev. A* **68**, 012709 (2003).
- [15] F. Lépine, C. Bordas, C. Nicole, and M. J. J. Vrakking, *Phys. Rev. A* **70**, 033417 (2004).
- [16] G. Lantoine and R. P. Russell, *Celest. Mech. Dyn. Astr.* **109**, 333 (2011).
- [17] H. A. Bethe and E. E. Salpeter, *Quantum Mechanics of One- and Two-Electron Atoms* (Springer, New York, 1957).
- [18] L. D. Landau and E. M. Lifshitz, *Quantum Mechanics: Non-Relativistic Theory* (Addison-Wesley, Reading, 1965).
- [19] T. F. Gallagher, *Rydberg Atoms* (Cambridge University Press, Cambridge, 1994), and references therein.
- [20] *Handbook of Mathematical Functions with Formulas, Graphs, and Mathematical Tables*, edited by M. Abramowitz and I. A. Stegun (Dover Publications, New York, 1965).
- [21] A. S. Stodolna, F. Lépine, A. Rouzée, S. Cohen, A. Gijsbertsen, J. H. Jungmann-Smith, C. Bordas, and M. J. J. Vrakking, *J. Phys. B* **50**, 164001 (2017).
- [22] L. B. Zhao and J. B. Delos, *Phys. Rev. A* **81**, 053418 (2010).
- [23] R. R. Freeman, N. P. Economou, G. C. Bjorklund, and K. T. Lu, *Phys. Rev. Lett.* **41**, 1463 (1978); R. R. Freeman, and N. P. Economou, *Phys. Rev. A* **20**, 2356 (1979); T. S. Luk, L. DiMauro, T. Bergeman, and H. Metcalf, *Phys. Rev. Lett.* **47**, 83 (1981).
- [24] H. Rottke and K. H. Welge, *Phys. Rev. A* **33**, 301 (1986).
- [25] E. Luc-Koenig and A. Bachelier, *J. Phys. B* **13**, 1743 (1980); **13**, 1769 (1980); V. V. Kolosov, *JETP Lett.* **44**, 588 (1986); T. P. Grosdanov, P. S. Krstić, and M. J. Raković, *Phys. Lett. A* **132**, 262 (1988); A. K. Kazansky, V. N. Ostrovsky, and D. A. Telnov, *J. Phys. B: At. Mol. Opt. Phys.* **23**, L433 (1990).
- [26] A. V. Gets and O. I. Tolstikhin, *Phys. Rev. A* **87**, 013419 (2013); S. Ohgoda, O. I. Tolstikhin, and T. Morishita, *ibid.* **95**, 043417 (2017).
- [27] W. H. Press, S. A. Teukolsky, W. T. Vetterling and B. P. Flannery, *Numerical Recipes in C: The Art of Scientific Computing* (Cambridge University Press, New York, 1992); T. H. Cormen, C. E. Leiserson, R. L. Rivest, and C. Stein, *Introduction to Algorithms*, 2nd ed. (MIT Press, Cambridge MA, 2001), Chap. 30.
- [28] R. B. Blackman and J. W. Tukey, *The Measurement of Power Spectra* (Dover Publications, New York, 1958).
- [29] Q. Z. Xia, J. F. Tao, J. Cai, L. B. Fu, and J. Liu, *Phys. Rev. Lett.* **121**, 143201 (2018); S. Brennecke and M. Lein, *Phys. Rev. A* **100**, 023413 (2019); S. D. López and D. G. Arbó, *ibid.* **100**, 023419 (2019).
- [30] A. Maquet, J. Caillat, and R. Taieb, *J. Phys. B* **47**, 204004 (2014); R. Gaillac, M. Vacher, A. Maquet, R. Taieb, and J. Caillat, *Phys. Rev. A* **93**, 013410 (2016).